Energy flux of nonlinear internal waves in northern South China Sea

Ming-Huei Chang,[1] Ren-Chieh Lien,[2] Tswen Yung Tang,[1] Eric A. D'Asaro,[2] and Yiing Jang Yang[3]

Received 15 November 2005; revised 13 December 2005; accepted 21 December 2005; published 4 February 2006.

[1] We analyze three sets of ADCP measurements taken on the Dongsha plateau, on the shallow continental shelf, and on the steep continental slope in the northern South China Sea (SCS). The data show strong divergences of energy and energy flux of nonlinear internal waves (NLIW) along and across waves' prevailing westward propagation path. The NLIW energy flux is 8.5 kW m^{-1} on the plateau, only 0.25 kW m^{-1} on the continental shelf 220 km westward along the propagation path, and only 1 kW m^{-1} on the continental slope 120 km northward across the propagation path. Along the wave path on the plateau, the average energy flux divergence of NLIW is $\sim$0.04 W m^{-2}, which corresponds to a dissipation rate of O(10^{-7}–10^{-6}) W kg^{-1}. Combining the present with previous observations and model results, a scenario of NLIW energy flux in the SCS emerges. NLIWs are generated east of the plateau, propagate predominantly westward across the plateau along a beam of $\sim$100 km width that is centered at $\sim$21°N, and dissipate nearly all their energy before reaching the continental shelf.
Citation: Chang, M.-H., R.-C. Lien, T. Y. Tang, E. A. D'Asaro, and Y. J. Yang (2006), Energy flux of nonlinear internal waves in northern South China Sea, *Geophys. Res. Lett.*, *33*, L03607, doi:10.1029/2005GL025196.

1. Introduction

[2] Satellite images show that nonlinear internal waves (NLIWs) are active in the northern South China Sea (SCS) between the Luzon Strait and the continental shelf (Figure 1a) [*Hsu and Liu*, 2000; *Zhao et al.*, 2004]. Most of the long-crested, multiple-wave packets exist in a 200 × 200 km^2 area on the plateau that includes Dongsha Island, hereafter referred to as the Dongsha plateau (Figure 1a). NLIWs on the northern continental slope and the Dongsha plateau have been described with in situ measurements by *Ramp et al.* [2004] and *Yang et al.* [2004].

[3] NLIW generation sites and mechanisms have not been identified. *Ebbesmeyer et al.* [1991] and *Ramp et al.* [2004] suggest that NLIWs are generated between the Batan Islands in the Luzon Strait, and propagate westward across the basin, the continental slope, and onto the continental shelf. *Lien et al.* [2005] suggest that internal tides are generated in the Luzon Strait, propagate across the basin in a narrow tidal beam, are amplified by the shoaling continental slope east of the Dongsha plateau, become nonlinear, and evolve into multiple wave packets. On the continental shelf west of the Dongsha plateau, NLIWs disintegrate; satellite images show fewer occurrences and shorter crest lines, suggesting that NLIWs dissipate most of their energy before reaching the continental shelf. However, no evidence from in-situ measurements has been documented.

[4] Here, we will compute the energy and energy flux on the plateau, on the continental shelf, and on the continental slope using ADCP measurements. We discuss the energy flux divergence and the implication of the energy dissipation rate of NLIWs in the northern SCS.

2. Mooring Positions and Instruments

[5] Two upward-looking, moored, 150-kHz broadband ADCPs (IW1 and IW3) and one upward-looking, bottom-mounted, 300-kHz ADCP (IW2) were deployed in the SCS in spring 2000 (Figure 1). IW1 was located on the eastern edge of the Dongsha plateau, IW2 on the continental shelf, and IW3 on the steep continental slope. IW1 and IW2 were positioned roughly along the propagation path of NLIWs. At IW1 and IW3, ADCPs were mounted at depths of 237 m and 248 m, respectively (Table 1). The bin size of ADCP data was 10 m for IW1 and IW3, and 5 m for IW2. All ADCP measurements were recorded every 1 min for about 20 days.

3. Internal Wave Energy

[6] Kinetic energy, potential energy, and the total energy are estimated using ADCP measurements. The principal characteristics of velocity spectra have been discussed by *Lien et al.* [2005]. Three primary spectral peaks are at the diurnal, the semidiurnal, and the compound tidal frequency bands. NLIWs are associated with a spectral bump in $0.001\ s^{-1} < \omega < N$; it is the most prominent in the vertical velocity spectrum, where ω is the frequency and N the buoyancy frequency.

[7] The potential energy spectrum Φ_{PE} is computed using the linear internal wave relation $\Phi_{PE} = \frac{N^2(\omega^2 - f^2)}{(N^2 - \omega^2)(\omega^2 + f^2)}(\Phi_u + \Phi_v)$, where Φ_u and Φ_v are the zonal and meridional velocity spectra, respectively, and f is the inertial frequency. The potential and the kinetic energy of NLIWs, semidiurnal tides, and diurnal tides are computed by integrating potential energy and velocity spectra over the corresponding frequency bands, chosen as $6.3 \times 10^{-5}\ s^{-1} < \omega < 8.3 \times 10^{-5}\ s^{-1}$ for the diurnal tide, $1.3 \times 10^{-4}\ s^{-1} < \omega < 1.6 \times 10^{-4}\ s^{-1}$ for the semidiurnal tide, and $10^{-3}\ s^{-1} < \omega < N$ ($\sim$0.02 s^{-1}) for the NLIW.

[1]Institute of Oceanography, National Taiwan University, Taipei, Taiwan.
[2]Applied Physics Laboratory, University of Washington, Seattle, Washington, USA.
[3]Department of Marine Science, Chinese Naval Academy, Kaohsiung, Taiwan.

0094-8276/06/2005GL025196$05.00

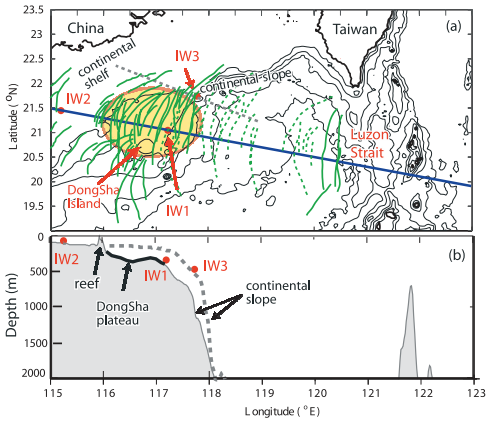

Figure 1. Map of the South China Sea, ADCP locations, summary of satellite images, and bathymetry. (a) Green curves are signatures of nonlinear internal waves shown on satellite images compiled by *Zhao et al.* [2004]. Red dots indicate locations of three ADCP stations. Black curves are isobaths of 200, 500, 1000, 2000, and 3000 m. The yellow region with the red outline represents the Dongsha plateau. (b) The bathymetry along the solid and dashed lines in Figure 1a. The thick solid curve west of IW1 represents the bottom of the Dongsha plateau. The array of reefs on the continental shelf break between IW1 and IW2, and the continental slope are shown by arrows.

Frequency bandwidths are determined by examining the observed energy spectra.

[8] The depth-integrated total energy E of the diurnal tide, the semidiurnal tide, and the NLIW is computed as $E = \overline{\rho} \int (\frac{1}{2}U^2 + \frac{1}{2}V^2 + \frac{1}{2}W^2 + PE)dz$, where $\overline{\rho}$ is the water density, U^2, V^2, and W^2 are zonal, meridional, and vertical velocity variances, respectively, computed by integrating spectra over the corresponding frequency bands. At IW2, ADCP measurements were taken in nearly the entire water column. At IW1 and IW3, however, measurements were taken only between 30 m and 210 m, missing measurements in more than one-half of the water column. To estimate the depth-integrated energy, the vertical normal modal structure is used. We use the non-hydrostatic eigen-mode equation for better representing the high-frequency NLIW. On average, about 70% of the observed velocity variances are explained by the first two modes at the three stations. The horizontal kinetic energy, the vertical kinetic energy, and the potential energy of the baroclinic component are estimated for the entire water column using the results of the modal decomposition and are vertically integrated (Table 1 and Figure 2).

[9] To assess the error associated with the modal decomposition at IW1 and IW3, we take advantage of the velocity measurements at IW2 that cover nearly the entire water column. We assume that IW2 measurements were taken only in the upper water column between 20 and 50 m, which is a similar proportion of the water column of IW1 and IW3 measurements, and use the vertical normal modal structure to estimate the depth-integrated total energy. The estimates are −15% of the true values for NLIWs, +4% for semidiurnal tides, and +50% for diurnal tides. We expect similar errors for estimates of the total energy at IW1 and IW3.

[10] The depth-integrated total energy of NLIWs is the greatest at IW1 (Table 1). Previous studies show that IW1 and IW2 are on the NLIW propagation path [*Yang et al.*, 2004; *Lien et al.*, 2005]. The total energy of NLIW at IW2 is only 8% of that observed at IW1, suggesting 92% of NLIW energy is lost between IW1 and IW2. This may be due to the horizontal spreading of NLIWs, the energy cascade from NLIWs to tides, or dissipation. Satellite images (Figure 1) show little horizontal spreading of NLIWs from IW1 to IW2, and there is no report of an energy cascade from NLIWs to tides. We propose that 4.4 kJ m^{-2} of the NLIW energy is dissipated across the plateau. The NLIW energy at IW3 is only 45% of that at IW1, consistent with fewer NLIWs at IW3 in satellites images, implying inhomogeneous NLIW energy distribution (Figure 1).

[11] The depth-integrated total energy of the semidiurnal and diurnal tides is the strongest at IW1 (Table 1). For IW1 and IW3, the semidiurnal tidal energy is greater than that of the diurnal tide. The diurnal and semidiurnal tidal energy at IW1 are about 10 times of those at IW2 and about 1.5 times of those at IW3. At IW1 the NLIW energy is greater than that of the tides.

4. Internal Wave Energy Flux

[12] We compute the vertically integrated energy flux using two independent methods: $\overline{F} = \int \overline{C}_g \, Edz$ and $\overline{F} = \int \langle p'\overrightarrow{u}' \rangle \, dz$, where p' and $\overrightarrow{u}'$ are the internal-

Table 1. Vertically Integrated Energy and Energy Flux of the NLIW (E_{NLIW}, and F_{NLIW}), of the Semidiurnal Tide (E_M and F_M), and of the Diurnal Tide (E_S and F_S)[a]

	E_{NLIW}, (kJ m^{-2})	E_M, (kJ m^{-2})	E_S, (kJ m^{-2})	F_{NLIW} kWm^{-1}	F_{NLIW} Θ, deg	F_M kW m^{-1}	F_M Θ, deg	F_S kWm^{-1}	F_S Θ, deg
IW1: 21° 2.77′N, 117° 13.17′E, 426 m	**4.75**	3.28	2.98	**8.5** **(7.5)**	**173** **(170)**	5.15 [11.3]	175 [168]	6.24	204
IW3: 21° 44.53′N, 117° 46.31′E, 468 m	**2.07**	2.47	1.82	**1.0** **(0.74)**	**140** **(141)**	4.1 [4.5]	172 [145]	4.18	115
IW2: 21°26.77′N, 115°11.43′E, 103 m	**0.36**	0.22	0.34	**0.25** **(0.11)**	**149** **(139)**	0.13 [0]	135	0.26	131

[a]The energy flux is shown in magnitude and the direction θ in degrees counterclockwise from the east. The positions and the water depth of the ADCP stations are shown in the first column. The energy flux of NLIWs computed using the pressure-velocity correlation method $\int \langle p'\overrightarrow{u}' \rangle \, dz$ is shown within parentheses. The energy flux of semidiurnal tide according to *Niwa and Hibiya*'s [2004] numerical model is shown in squared brackets. NLIW energy and energy flux are in bold face.

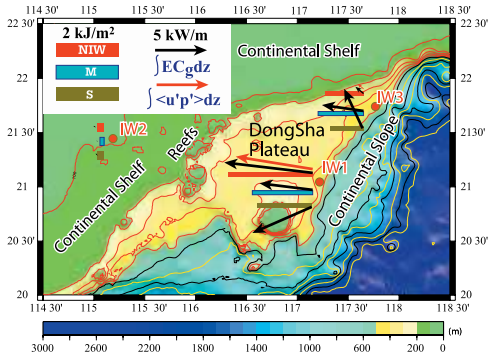

Figure 2. Vertically integrated energy and energy flux. Horizontal bars represent vertically integrated energy of NLIWs (red), semidiurnal tides (M) (blue), and diurnal tides (S) (green-grey). Black and red arrows represent vertically integrated energy flux computed as $\vec{F} = \int \vec{C}_g\, Edz$ and $\vec{F} = \int \langle p'\vec{u}' \rangle\, dz$, respectively. Values of the energy flux at IW2 are small, nearly invisible at this scale.

wave-induced pressure and velocity vector, respectively, $\vec{C}_g$ the group velocity, and $\langle\ \rangle$ the ensemble average. In the first method, the total energy estimated in section 3 is used. For the semidiurnal tide we determine the energy speed as $\vec{C}_g = \frac{N^2 - \omega^2}{N^2}\vec{C}_p$, where $\vec{C}_p$ is the phase velocity. The phase velocity is obtained by the vertical normal mode analysis.

[13] For NLIWs the intrinsic nonlinearity might violate the above relation of linear internal waves. The group speed of NLIWs inferred by *Lien et al.* [2005] is adopted. The direction of the group velocity is determined using the harmonic analysis; that is, $\vec{u}'(z, t) = A(z)\cos(\omega t) + B(z)\sin(\omega t) + R(z)$, where $\vec{u}'(z)$ is the baroclinic horizontal velocity vector. We minimize the sum of the squares of the residual $R(z)$ to obtain $A(z)$ and $B(z)$. The major axis of the current ellipse is determined using $A(z)$ and $B(z)$. The direction of the major axis of the velocity vector in the upper 100 m at IW1 and IW3 and that in the upper 50 m at IW2 are used to determine the flux direction, better representing the lowest two modes of internal waves.

[14] We also compute the energy flux as $\vec{F} = \int \langle p'\vec{u}' \rangle dz$ following *Nash et al.* [2005]. The $\vec{u}'$ and p' are expressed as follows,

$$p'(z,t) = p_{surf}(t) + \int_z^0 \rho'(z,t) g dz, \tag{1}$$

$$\vec{u}'(z,t) = \vec{u}(z,t) - \bar{\vec{u}}(z) - \bar{\vec{u}}_0(t), \tag{2}$$

where ρ' is the density anomaly, p_{surf} the surface pressure, $\vec{u}(z, t)$ the instantaneous velocity, $\bar{\vec{u}}(z)$ the time mean of velocity, and $\bar{\vec{u}}_0(t)$ is determined by the baroclinicity condition $\frac{1}{H}\int_{-H}^{0} \vec{u}'(z,\ t)dz = 0$. Surface pressure p_{surf} is also determined by the baroclinicity condition, $\frac{1}{H}\int_{-H}^{0} p'(z,\ t)dz = 0$. The ρ' is estimated as $\rho'(z,\ t) = (\bar{\rho}/g)\overline{N}^2\ \xi(z,\ t)$, where $\xi(z,\ t)$ is isopycnal displacement and is computed by the time integration of vertical velocity, $\xi(z,\ t) = \int_0^t w(z,\ \tau)d\tau$. To satisfy the baroclinicity conditions of $\vec{u}'$ and p', data from the entire water column are needed. Again, we use results of the vertical structures of velocity and displacement determined by the normal mode analysis outside of the ADCP measurement depths.

[15] There are two sources of error for the calculation of the energy flux: the inference of perturbation pressure p' from the vertical velocity and the inference of $\vec{u}'$ in the entire water column using the normal mode analysis. The vertical velocity measurements might suffer from instrument noise and biological interference. For linear internal waves, the ratio of the vertical velocity spectrum Φ_w to the horizontal velocity spectrum $\Phi_u + \Phi_v$ should satisfy the consistency relation $\frac{\Phi_w}{\Phi_u + \Phi_v} = \frac{\omega^2(\omega^2 - f^2)}{(N^2 - \omega^2)(\omega^2 + f^2)}$ [*Lien and Müller*, 1991]. The observed ratio $\frac{\Phi_w}{\Phi_u + \Phi_v}$ agrees with the theoretical relation for $\omega > 2.3 \times 10^{-4}$ s^{-1}, including the NLIW frequency band suggesting w in the NLIW band is the oceanic signal. The consistency test fails for the semidiurnal and diurnal tides. Here the calculation of the energy flux $\langle p'\vec{u}' \rangle$ applies for NLIWs only.

[16] Using IW2 measurements, we assess the errors of using the vertical structures from the normal mode analysis to compensate for missing measurements in the water column at IW1 and IW3 following the technique as described in section 3. The estimated energy flux is about 12% less than the true energy flux for NLIWs.

[17] The estimate of displacements $\xi(z, t)$ of NLIWs is 50–110 m at IW1, 10–60 m at IW3, and 5–25 m at IW2, consistent with previous results [*Lien et al.*, 2005]. The NLIW energy flux computed from two methods are in good agreement (Figure 2 and Table 1). At IW1, the vertically integrated NLIW energy flux is 8.5 kWm^{-1}, about 34 times that at IW2 and 8.5 times that at IW3 based on the energy method $\vec{F} = \int \vec{C}_g\, Edz$. The pressure-velocity correlation method $\vec{F} = \int \langle p'\vec{u}' \rangle dz$ yields similar results (Table 1). The NLIW energy flux propagates nearly westward at IW1, and northwestward at IW2 and IW3.

[18] The estimated semidiurnal tidal energy flux is westward 5.15 kW m^{-1} at IW1. This is only one-half that of *Niwa and Hibiya*'s [2004] model result at the same location. We offer several possible explanations for the discrepancy. First, Niwa and Hibiya's model is hydrostatic with a horizontal spatial resolution of ~3 km, and therefore, does not produce NLIW that is non-hydrostatic and has a horizontal scale of 1–2 km. In reality, we expect that some of tidal energy flux is converted to NLIW energy flux. The data supports this idea; the model semidiurnal tidal energy flux is nearly equal to the sum of our estimates of NLIW and semidiurnal tidal energy flux. Alternatively, Niwa and Hibiya's model uses the climatological stratification and

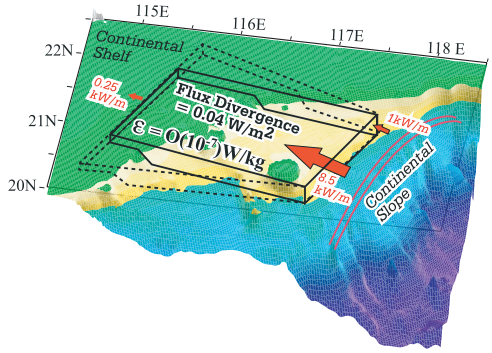

Figure 3. Flux divergence of nonlinear internal waves on the plateau. The average dissipation rate is calculated as $\varepsilon = \frac{\Delta F}{\Delta s}$, where ΔF is the difference between vertically integrated energy fluxes at IW1 and IW2, and Δs is the distance between IW1 and IW2. The flux divergence is about 0.04 W m^{-2}, corresponding to a dissipation rate of $O(10^{-7})$ W kg^{-1}. The dashed-line and solid-line boxes illustrate the horizontal spreading of nonlinear internal wave energy.

does not include the Kuroshio. In reality, the internal tidal energy flux and the tidal beam should be modulated by the fluctuations of the Kuroshio, the stratification, the shear, and meso-scale eddies in the SCS. Averaging the model results between 20 and 22°N along 117°E yields a mean model semidiurnal tidal energy flux of 5 kW m^{-1}, similar to our estimates. Finally, our estimates of the energy flux may have substantial error considering that we have to rely on the solution of the normal mode analysis.

[19] The diurnal and semidiurnal tide energy fluxes have a similar magnitude. Our analysis and the numerical model conclude that the semidiurnal tidal energy flux is concentrated in a narrow westward tidal beam, whereas the diurnal tidal beam is wider.

5. Energy Flux Divergence and Dissipation Rate

[20] The energy flux of NLIWs decreases dramatically from IW1 to IW2. Here, the dissipation rate is inferred from the energy flux divergence.

[21] The equation of energy conservation can be expressed as follows,

$$\frac{\partial E}{\partial t} + (u \cdot \nabla)E = \nabla \cdot F - \varepsilon, \tag{3}$$

where E is the total energy and ε is the dissipation rate of kinetic energy. Assuming that the nonlinear advection and the local time rate of change are small, the above equation may be rewritten as $0 = \frac{\partial}{\partial s}F - \varepsilon$. The average dissipation rate is $\varepsilon = \frac{\Delta F}{\Delta s}$, where ΔF is the difference of the energy fluxes at IW1 and IW2, and Δs is the distance between IW1 and IW2, ~220 km. IW1 and IW2 are roughly aligned with the NLIW propagation path. The average energy flux divergence is ~0.04 W m^{-2}. As discussed in section 3, we propose that the energy flux divergence is due to the dissipation and obtain an estimate of ε of $O(10^{-7})$W kg^{-1}over an average of 250-m water depth (Figure 3). If most of the dissipation occurs at 10-m thick layers, ε would be 4×10^{-6} W kg^{-1}, agreeing with the previous estimate [*Lien et al.*, 2005]. The horizontal spreading of NLIWs could cause the loss of the energy density. According to satellite images (Figure 1), the spreading of NLIW crest lines is no more than a factor of two from IW1 to IW2. Our estimate of ε should be accurate within a factor of two (Figure 3).

[22] The divergence of the semidiurnal tidal energy is 0.023 kW m^{-2} between IW1 and IW2, similar to *Niwa and Hibiya*'s [2004] model result after averaging between 20 and 22°N.

6. Discussion and Summary

[23] Dongsha Island is located on the southeast corner of a plateau of 300–500-m depth (Figure 2). There is a steep continental slope on the east of the plateau connected to the deep basin of the SCS, and a secondary slope on the west of the plateau connected to the continental shelf. An array of shallow reefs is present near the shelf break. The plateau is bounded by a steep continental slope on the north connected to the continental shelf and opened to a gradual slope on the south connected to the deep basin. NLIWs and internal tides are strongly affected by this complex topography and the presence of Dongsha Island, resulting in NLIW reflection, refraction, diffraction, and interactions [*Lynett and Liu*, 2002].

[24] NLIW energy flux coming from the east squeezes into the plateau, and results in a strong energy flux at IW1, and much smaller energy flux at IW3. A cross-correlation analysis shows a significant correlation between the NLIW vertical kinetic energy at IW1 and IW3. The presence of the Dongsha plateau directs the internal tidal beam to propagate onto the plateau and substantially converts to NLIWs, whereas the lack of the plateau west of IW3 blocks the internal tidal beam and results in weaker NLIWs.

[25] On the continental shelf west of the plateau the energy flux is only 1/30 of the energy flux on the eastern edge of the plateau. A cross-correlation analysis shows no significant correlation between NLIW energy at IW2 and IW1. The reef array on the shelf break west of the plateau is as shallow as 50 m (Figure 2). Even if NLIWs at IW2 indeed originate from IW1, very little NLIW energy from IW1 arrives at IW2, and the presence of the reef array might destroy the wave relation. The continental shelf break may be another generation source for NLIW observed at IW2.

[26] Our analysis based on in-situ measurements combined with previous observations and model results suggest a scenario of NLIW energy flux in the SCS (Figure 3). NLIWs are generated somewhere east of the Dongsha plateau, propagate predominantly westward along a narrow beam of ~100-km width, and dissipate nearly all of their energy across the plateau before reaching the continental shelf. The average NLIW energy flux divergence across the plateau is 0.02–0.04 W m^{-2}. The dissipation rate of NLIWs averaged over the water column is $O(10^{-7}-10^{-6})$ W kg^{-1}. The divergence of NLIW energy flux across the plateau is greater than that of the semidiurnal tide, suggesting that

NLIWs are the main process responsible for the transfer of internal tidal energy to turbulence mixing.

[27] **Acknowledgments.** We thank Y. Niwa and T. Hibiya for providing their model results of internal tidal energy flux. We would like to thank Oliver Fringer for providing helpful comments. This work is supported by the ONR grant N00014-04-1-0237 and by the National Science Council of Taiwan.

References

Ebbesmeyer, C. C., C. A. Coomes, and R. C. Hamilton (1991), New observations on internal waves (solitons) in the South China Sea using acoustic Doppler current profiler, paper presented at Mar. Technol. Soc. 91 proceedings, New Orleans, 165–175.

Hsu, M.-K., and A. K. Liu (2000), Nonlinear internal waves in the South China Sea, *Can. J. Remote Sens.*, *26*, 72–81.

Lien, R.-C., and P. Müller (1991), Consistency relations for gravity and vertical modes in the Ocean, *Deep Sea Research, Part A*, *39*, 1595–1612.

Lien, R.-C., T. Y. Tang, M. H. Chang, and E. A. D'Asaro (2005), Energy of nonlinear internal waves in the South China Sea, *Geophys. Res. Lett.*, *32*, L05615, doi:10.1029/2004GL022012.

Lynett, P., and P. L.-F. Liu (2002), A two-dimensional, depth-integrated model for internal wave propagation, *Wave Motion*, *36*, 221–240.

Nash, J. D., M. H. Alford, and E. Kunze (2005), On estimating internal wave energy fluxes in the ocean, *J. Atmos. Oceanic Technol.*, *22*, 1551–1570.

Niwa, Y., and T. Hibiya (2004), Three-dimensional numerical simulation of M_2 internal tides in the East China Sea, *J. Geophys. Res.*, *109*, C04027, doi:10.1029/2003JC001923.

Ramp, R. S., T. Y. Tang, T. F. Duda, J. F. Lynch, A. K. Liu, C.-S. Chiu, F. Bahr, H.-R. Kim, and Y. J. Yang (2004), Internal solitons in the northeastern South China Sea, part I: Source and deep water propagation, *IEEE J. Oceanic Eng.*, *29*, 1157–1181.

Yang, Y. J., T. Y. Tang, M. H. Chang, A. K. Liu, M.-K. Hsu, and S. R. Ramp (2004), Solitons northeast of Tung-Sha Island during the ASIAEX pilot studies, *IEEE J. Oceanic Eng.*, *29*, 1182–1199.

Zhao, Z., V. Klemas, Q. Zheng, and X.-H. Yan (2004), Remote sensing evidence for baroclinic tide origin of internal solitary waves in the northeastern South China Sea, *Geophys. Res. Lett.*, *31*, L06302, doi:10.1029/2003GL019077.

E. A. D'Asaro and R.-C. Lien, Applied Physics Laboratory, University of Washington, Seattle, WA 98105, USA. (lien@apl.washington.edu)

M.-H. Chang and T. Y. Tang, Institute of Oceanography, National Taiwan University, Taipei 106, Taiwan.

Y. J. Yang, Department of Marine Science, Chinese Naval Academy, Kaohsiung 813, Taiwan.